P and S wave finite-frequency tomography reveals the impact of slab interference on mantle flow beneath the greater Alpine region

Mao Yuantong, Tang Xiaotian, Zhao Liang, Malusà Marco G., Guillot Stéphane, Paul Anne, Solarino Stefano, Xiaobing Xu, Aubert Coralie, Eva Elena, et al.

▶ **To cite this version:**

Mao Yuantong, Tang Xiaotian, Zhao Liang, Malusà Marco G., Guillot Stéphane, et al.. P and S wave finite-frequency tomography reveals the impact of slab interference on mantle flow beneath the greater Alpine region. Earth and Planetary Science Letters, 2025, 673, pp.119716. ⟨10.1016/j.epsl.2025.119716⟩. ⟨hal-05344547⟩

HAL Id: hal-05344547

https://hal.science/hal-05344547v1

Submitted on 3 Nov 2025

HAL is a multi-disciplinary open access archive for the deposit and dissemination of scientific research documents, whether they are published or not. The documents may come from teaching and research institutions in France or abroad, or from public or private research centers.

L'archive ouverte pluridisciplinaire **HAL**, est destinée au dépôt et à la diffusion de documents scientifiques de niveau recherche, publiés ou non, émanant des établissements d'enseignement et de recherche français ou étrangers, des laboratoires publics ou privés.

HAL Authorization

P and S wave finite-frequency tomography reveals the impact of slab interference on mantle flow beneath the greater Alpine region

Yuantong Mao, Xiaotian Tang, Liang Zhao*, Marco G. Malusà*, Stéphane Guillot, Anne Paul, Stefano Solarino, Coralie Aubert, Elena Eva, Silvia Pondrelli, Simone Salimbeni, Lei Yang

Abstract

The Cenozoic evolution of the tortuous Adria-Europe plate boundary zone suggests potential interference between opposite-dipping slabs in the upper mantle, with potential perturbation of the surrounding mantle flow. However, compelling seismic evidence of slab interference beneath the greater Alpine region is still lacking. Here we use P- and the first S-wave velocity models based on the Finite-Frequency Tomography method to reveal the interactions between slabs imaged beneath the greater Alpine region and their relationships with prominent low-velocity anomalies in the upper mantle. We document high-velocity anomalies beneath the Alps, the Apennines and the northern Dinarides. Low-velocity anomalies are found to the west of the Alps, beneath the Po Plain, and on either side of the central-southern Apennines. Because of slab interference, low-velocity anomalies of different origins, either due to asthenospheric upwelling or slab fluids, coexist in nearby regions of the upper mantle. The lack of slab gaps between the Western Alps slab and the retreating Apenninic slab precludes potential toroidal flow around the northern tip of the Apenninic slab during slab rollback, with consequent activation of an asthenospheric counterflow and associated mantle upwelling to the west of the Alps. Beneath the Eastern Alps, the Alpine slab is torn and overturned by the NE-dipping Dinaric slab. The asthenospheric mantle beneath the Po Plain is confined by slabs and shows a prominent low-velocity anomaly likely due to melting triggered by carbon-rich supercritical fluids generated above the Alpine slab. Toroidal flow may occur farther south around the Apenninic slab, in a region where the mantle flow is not affected by interaction between slabs. Similar complexities may characterize other plate-boundary zones where the interplay between opposite-dipping slabs is suggested by geophysical and geological data, such as Taiwan or the Hindu Kush - Pamir - Tianshan tectonic knot in Central Asia.

1. Introduction

The greater Alpine region has been shaped during Cretaceous to present convergence between the European plate and the Adriatic microplate (Dewey et al., 1989; Jolivet and Faccenna, 2000; Handy et al., 2010; Malusà et al., 2015). It includes several orogenic belts, such as the Alps, the Apennines and the Dinarides (Fig. 1), overlying a complex and still debated slab structure (e.g., Lippitsch et al., 2003; Piromallo and Morelli, 2003; Koulakov et al., 2009; Giacomuzzi et al., 2011; Zhao et al., 2016a; Paffrath et al., 2021; Rappisi et al., 2022; Kästle et al., 2025). These slabs are thought to control the flow pattern in the surrounding asthenospheric mantle (Barruol et al., 2004; Vignaroli et al., 2008; Jolivet et al., 2009; Baccheschi et al., 2024), which in turn has a major impact on the topography of the region (Faccenna and Becker, 2010; Salimbeni et al., 2018; Sternai et al., 2019).

The geologic evolution of the Adria-Europe plate boundary zone, characterized by protracted northward motion of Adria relative to Europe (Fig. 1a), supports the hypothesis of slab interference at depth, which is expected to affect the surrounding mantle flow. However, compelling seismic evidence of slab interference is still lacking, and would require higher-resolution seismic tomography models. Based on available geological constraints, regions of potential slab interaction are located in the Alps-Apennines transition zone, where interaction between the Western Alps slab and the retreating Apenninic slab may have controlled the location of the rotation pole of the Corsica-Sardinia block (Gattacceca et al., 2007; Malusà et al., 2016), and in the transition zone between the Eastern Alps and the Dinarides, where the northward motion of the Dinaric slab may have induced tearing of the Alpine slab (Ji et al., 2019; Mosconi et al., 2024). Some tomographic studies did document a subduction polarity reversal from the Central Alps to the Eastern Alps (Zhao et al., 2016a; Kästle et al., 2020; Paffrath et al., 2021), but the European vs. Adriatic origin of the slab beneath the Eastern Alps remains unclear (Koulakov et al., 2009; Malusà et al., 2021; Jozi Najafabadi et al., 2022).

To shed light on these issues, here we present a higher-resolution teleseismic P-wave finite-frequency tomography model and the first S-wave tomography model of the Alpine region based the denser seismic datasets never used in the Alps coming from permanent networks and temporary stations of the AlpArray (Hetenyi et al., 2018) and CIFALPS and CIFALPS2 (Zhao et

al., 2016b; Zhao et al., 2018) seismic experiments. For crustal correction we also used the new AlpsLig-crust_WET model, which has a crustal resolution of 0.02° and was derived from ambient-noise wave-equation tomography (Nouibat et al., 2023). Our results provide unprecedented evidence of slab interactions beneath the greater Alpine region, which are discussed for their impact on asthenospheric mantle flow and associated geologic processes in the upper mantle, with potential application to other complex plate-boundary zones worldwide.

2. Data and Methods

2.1 Data selection and analysis

The seismic datasets used in this study were collected from 1093 seismic stations deployed in the greater Alpine area from 2012 to 2020 (Fig. 1b). Compared to the tomography conducted by Zhao et al. (2016a), nearly twice as many seismic stations have been used, which include 659 permanent stations collected from the European Integrated Data Archive (EIDA) European archive (http://webdc.eu/webdc3/), 110 temporary broadband seismic stations from the dense arrays of the CIFALPS seismic experiments across the southern and northern Western Alps (Zhao et al., 2016b; Zhao et al., 2018), and 324 temporary stations from the AlpArray Seismic Network across the Alpine region (Hetenyi et al., 2018). As shown in Fig. 1b, both the Alps and the Apennines are well covered by seismic stations, although not all the stations operated continuously throughout this period under consideration, and only the Tyrrhenian Sea, the Adriatic Sea and the southern Dinarides have lower coverage. Within this framework, the abundance of seismic data available allowed us to select not only high-quality P-wave travel time residuals, but also S-wave travel time residuals for tomography.

We measured the travel time residuals relative to synthetic arrival times based on the IASPEI91 1D velocity model (Kennett and Engdahl, 1991) using CrazySeismic (Yu et al., 2017), an open-source software package that employs multi-channel cross-correlation (VanDecar and Crosson, 1990). Finite frequency theory postulates that seismic waveforms with different frequencies are sensitive to velocity anomalies of different scales (Dahlen et al., 2000; Hung et al., 2000), lower frequency waveforms being sensitive to larger scale structures, and higher frequency waveforms being sensitive to smaller scale structures. In this study, two different frequency bands were selected for both P and S waves, that is 0.1-0.5 Hz and 0.5-2 Hz for P waves, and 0.05-0.1 Hz and 0.1-0.5 Hz for S waves. To ensure data quality for tomography, the following three criteria

were applied in event selection and travel time residual measurements: (1) selected teleseismic events have magnitude > 5 and epicentral distances between 30° and 90°; (2) each selected event is recorded by a minimum of 50 stations and includes high-quality waveforms from the reference station DAVOX, to ensure that the relative travel time residuals reflect variations in velocity anomalies rather than inconsistencies due to uneven station recording over a long-time interval; (3) relative travel time is less than three standard deviations of the total dataset. The number of seismic events and traveltime residuals selected for inversion across different frequency bands are listed in Supplementary Table S1. More than 200,000 P-waveforms and 100,000 S-waveforms in total were collected, resulting in a substantial dataset. The distribution of events is shown in Fig. 1c. Examples of selected waveforms are shown in Supplementary Figs. S1 and S2.

We analyzed travel time residuals for seismic events from various back-azimuths (Supplementary Fig. S3). Residuals for both P and S waves exhibit consistent distribution. The region extending from the southern Western Alps to the French Central Massif shows late arrivals, the foreland area located northwest of the Western Alps shows early arrivals. The relative travel time residuals vary with ray azimuths, highlighting lateral heterogeneity in the crust and upper mantle.

2.2 Crustal correction

Previous studies already showed that the Alpine region is characterized by significant velocity heterogeneities in the upper crust and the mantle (Kästle et al., 2018; Solarino et al., 2018; Lu et al., 2020; Zhao et al., 2020; Monna et al., 2022; Nouibat et al., 2022; Paul et al., 2022; Kind et al., 2023; Nouibat et al., 2023; Solarino et al., 2024). In this teleseismic tomography study, to correct for the crustal heterogeneity for S waves, we utilized the AlpsLig-crust_WET model, which has a crustal resolution of 0.02° and was derived from ambient-noise wave-equation tomography (Nouibat et al., 2023). For regions outside the coverage of the AlpsLig-crust_WET model, the Eucrust_transD-ANT model was used instead, with a resolution of 0.15° (Nouibat et al., 2022) (Supplementary Fig. S4). High-resolution P-wave velocity crustal structures are usually obtained by local earthquake tomography (Solarino et al., 2018; Jozi Najafabadi et al., 2022; Solarino et al., 2024). However, due to the heterogeneous distribution of intermediate depth earthquakes in the Alpine region (e.g., Eva et al., 2020), the availability of crustal models based on the analysis of P waves is limited. Therefore, we used the S-wave crustal velocity

model scaled by 1.73 for P-wave crustal correction. We employed a 1D ray tracing algorithm to calculate crustal residuals beneath all stations, focusing on the crust and the uppermost mantle above 50 km depth, then subtracted these from the teleseismic travel time residuals. The crustal travel time residuals are shown in Supplementary Fig. S4. Orogenic belts generally exhibit travel time delays, while regions in the foreland, particularly the so-called Ivrea Body (at 7.5-8°E) (Closs and Labrouste, 1963), display travel time advances, which indicates that crustal correction may lead to more reliable imaging of the underlying upper mantle. After applying the refined velocity model for crustal correction, the imaging results show relevant changes, especially in the uppermost mantle beneath mountain belts. The P-wave and S-wave velocity images before and after crustal correction are presented in Supplementary Figs. S5 and S6, and show continuous high-velocity anomalies that become more pronounced after crustal correction, particularly at depths above 150 km.

2.3 Finite Frequency Tomography method

We used the finite-frequency tomography method (Dahlen et al., 2000; Hung et al., 2000) to image the velocity structure of the upper mantle. This approach accounts for the effects of velocity perturbations in the vicinity of the ray path, rather than assuming infinitely high-frequency ray paths, thus providing a more accurate representation of the impact of velocity structure on arrival times. The tomography model was parameterized as a uniform grid of 64×64×64 centered at 10°E, 45°N, with grid spacing of ~27.8 km in longitude, ~17.5 km in latitude, and ~25 km in depth. Then, inversion matrices were constructed separately from the P-wave and S-wave datasets based on the finite-frequency kernel formulation. We used the damped LSQR (Paige and Saunders, 1982) method to determine the damping factor by balancing the trade-off between the model norm and variance reduction. The damping factors used in this study, 100 for P waves and 140 for S waves, result in a variance reduction of approximately 85% for the P-wave model and 74% for the S-wave model (Supplementary Fig. S7).

2.4 Resolution model

Checkerboard tests were performed to evaluate model resolution by reconstructing synthetic models with known alternating high- and low-velocity anomalies, using the same source-receiver geometry as the actual data inversion. To simulate noise, 10% Gaussian white noise was added to the synthetic travel time residuals. Several checkboard scales were tested, with 4×4×4 (~110

km×70 km×100 km) and 5×5×5 (~139 km×88 km×125 km) grids ultimately chosen as optimal resolutions for P waves and S waves, respectively. The configurations in synthetic models used ±3% anomalies for P waves and ±5% anomalies for S waves. Synthetic arrival times were generated for the same event-station pairs as the observed data, and the models were compared to assess resolution in the upper mantle. The recovery models demonstrate good resolution for both P-wave and S-wave datasets, particularly in the Alps (Supplementary Figs. S8–S11). A reduced amplitude of velocity anomalies is observed in places in the checkerboard tests due to limited data coverage and the use of damping parameters in the inversion process, which is a common issue in seismic tomography studies (Lévêque et al., 1993; Rawlinson and Sambridge, 2003). In our results, achieving recovery within 2% to 3% of the input anomaly is considered a good resolution.

P waves, with their higher frequencies compared to S waves, are more effective at detecting smaller anomalies and offer better resolution. Beneath the Alps, the P-wave dataset effectively recovers the velocity structure in the uppermost 600 km. In contrast, S waves perform well in detecting larger anomalies in the uppermost 400 km. Beneath the Apennines, resolution is limited in places due to insufficient ray coverage. Only results from regions with good resolution are discussed in the next sections. Smearing effects are visible in both the depth slices and cross-sections, reflecting the preferential directions of seismic rays. More specific synthetic tests can be used to determine whether the observed inclined structures in cross-sections are due to the actual velocity structure or the uneven distribution of seismic rays. We thus performed synthetic tests to assess the model's ability to resolve gaps between slabs, which are described in Sect. 3.4.

3. Results

3.1. Main features of the P and S wave tomography models

Figures 2 and 3 illustrate the updated high-resolution perturbation velocity model for P waves, whereas Figs. 4 and 5 illustrate the newly developed perturbation velocity model for S waves. The P-wave tomography model is based on a more extensive dataset compared to previous work and includes accurate crustal corrections. In the horizontal depth slices of Fig. 2 are evident the high-velocity anomalies beneath the Alps, the Apennines and the northern Dinarides. Prominent low-velocity anomalies are found to the west of the Alps (L1), beneath the Po Plain (L2), and on either side of the high-velocity anomaly beneath the central-southern Apennines (L3 and L4)

(Fig. 2). The S-wave velocity model reveals similar high-velocity features, which are strongest beneath the Alps and the northern Apennines, and low-velocity anomalies L1 to L4 that are particularly prominent (Fig. 4). The high-velocity anomaly beneath the Apennines shows a gap at shallow depth in the S-wave tomography model at ~13.5°E (Fig. 3b). Five cross-sections A-A' to E-E' (Figs. 3, 5) traverse the high- and low-velocity anomalies detected in map view in the P- and S-wave tomography models in order to explore their relationships.

The cross-section A-A' traverses the Western Alps and the northernmost Apennines, reaching the eastern Po Plain (Fig. 3a). It reveals a broad high-velocity anomaly at depths of 150–300 km, which may be indicative of slab interference. Within this anomaly, the P-wave velocity model provides higher-resolution results, identifying a gap that likely reflects the presence of two distinct E-dipping slabs, the Western Alps slab (WA) to the west and the Apenninic slab (AP) to the east. These two slabs are also distinguishable in the S-wave velocity model (Fig. 5a). In both models, the Western Alps slab can be traced continuously to depths >400 km down to the mantle transition zone and even deeper. The broad low-velocity anomaly L1, located to the west of the Western Alps (Figs. 3a and 5a), extends at least from the mantle transition zone to the uppermost mantle, and exhibits a high amplitude especially in the S-wave velocity model (Fig. 5a). To the east, the cross-section A-A’ intersects the low-velocity anomaly L2 located beneath the Po Plain. In the S-wave tomography model, this anomaly is particularly evident in the depth range between 300 and 175 km depth (Fig. 5a).

The cross-section B-B' traverses the Central Alps (Fig. 3b) and shows a SE-dipping high-velocity anomaly interpreted as the Central Alps slab (CA). This can be traced down to the mantle transition zone and becomes shallow-dipping at ~300 km depth. Above the Central Alps slab lies the low-velocity anomaly L2, which exhibits high amplitude in both the P-wave and S-wave velocity models (Figs. 3b and 5b). Its depth is constrained to 150–300 km in the P-wave tomography model (Figs. 3b), and it is strongest in the S-wave tomography model in the depth range between 175 and 300 km.

The cross-section C-C’ traverses the Eastern Alps, the Po Plain, and the Northern Apennines (Figs. 3c and 5c). The high-velocity anomaly observed beneath the Eastern Alps is NE-dipping and extends to a depth of 600 km. It is notably broad in both the P-wave and S-wave velocity models, which may be indication of close spacing between interacting slabs. The Eastern Alps

slab (EA) lies to the north, and the Dinaric (DI) slab lies to the south. However, they are difficult to distinguish, especially in the S-wave model. To the SW, beneath the Po Plain, the low-velocity anomaly L2 lies on top of the Central Alps slab (CA). A continuous NE-dipping high-velocity anomaly is observed farther to the SW beneath the Apennines. It represents the Apenninic (AP) slab, which becomes SW-dipping at depths greater than 250 km. Above the high-velocity anomaly representing the Apenninic slab is the low-velocity anomaly L1.

The cross-sections D-D' and E-E' traverse the Apennines parallel to section C-C' (Figs. 3d, e and 5d, e). They show a continuous high-velocity anomaly ascribed to the Apenninic slab (AP). The anomaly is near-vertical in cross-section D-D', and SW-dipping in cross section E-E', reaching as deep as 600 km. The slab window described by previous work above 150 km depth beneath the central Apennines (Giacomuzzi et al., 2011; Zhao et al., 2016a) is exclusively observed in the S-wave tomography model along cross-section E-E' (Fig. 5e). Below 150 km depth, however, the high-velocity anomaly is continuous. Two low-velocity anomalies are detected on either side of the Apenninic slab, the anomaly L3 on the NE side, and the anomaly L4 on the SW side. The anomaly L3 extends below the slab from the mantle transition zone to ~100 km depth, whereas the anomaly L4 extends above the slab and at depth shallower than 300 km. It is weaker along cross-section D-D' compared to cross-section E-E' and apparently disconnected from anomaly L1.

3.2 Western Alps - Apennines transition zone

In the transition zone between the Western Alps and the Apennines, our high-resolution velocity model allows clear differentiation between the Western Alps slab and the Apenninic slab. Figure 6 illustrates three east-west profiles to further explore the relationship between these two slabs.

In the northernmost profile (Fig. 6a), the cross-section primarily intersects the Western Alps slab, which can be traced continuously from the Earth's surface down to a depth of at least 400 km. Another high-velocity anomaly, corresponding to the northern tip of the Apenninic slab is observed to the east of the Western Alps slab at depths of approximately 100–300 km. A velocity gap is evident between the two slabs, marked by a lower amplitude anomaly that highlights their separation. Although the P-wave velocity model offers higher resolution, a similar feature is also observed in the S-wave velocity model (Supplementary Fig. S13).

In the intermediate profile (Fig. 6b), both high-velocity anomalies are clearly defined. The Western Alps anomaly is predominantly located at depths of 200–400 km. It likely represents the southward continuation of the Western Alps slab, and it is thinned towards the Earth's surface. The Apenninic high-velocity anomaly is found to the east of the Western Alps slab, at depths of 100–300 km.

In the southernmost profile (Fig. 6c), the shallow portion of the Western Alps slab is no longer visible, as it is replaced by a prominent low-velocity anomaly (L1). Remnants of the high-velocity anomaly persist at depths of 300–400 km. This indicates the southern tip of the Western Alps slab, which reaches at least 44°N in map view. The Apenninic slab, in contrast, is visible from the uppermost mantle to depths of 300 km in the southernmost profile. This observation aligns well with the previously observed NE-dipping subduction of the Apenninic slab in Fig. 3c, offering further support to the hypothesis of an interaction between slabs in the Alps-Apennines transition zone.

3.3 Eastern Alps - Dinarides transition zone

Figure 7 illustrates four SSW-NNE profiles across the complex slab structure beneath the transition zone between the Eastern Alps and the Dinarides. The first and westernmost profile (Fig. 7a) lies to the west of the Giudicarie Line and exclusively intersects the SE-dipping Central Alps slab.

The second profile (Fig. 7b) is located to the east of the Giudicarie Line. It crosses a N-dipping high-velocity anomaly, which marks the Eastern Alps slab subducting northward into the mantle transition zone. Beneath the Po Plain, the Central Alps slab remains identifiable, with the low-velocity anomaly L2 lying above it. Along the third profile (Fig. 7c), the N-dipping high-velocity anomaly extends continuously into the mantle transition zone, reaching depths around 600 km. However, this high-velocity anomaly beneath the Eastern Alps is over 300 km wide, suggesting the combined interference of both the Eastern Alps and Dinaric slabs. Although no distinct velocity gap clearly separates the two slabs, the Eastern Alps slab is likely located to the north, and the Dinaric slab is positioned to the south. In the fourth and easternmost profile, the high-velocity anomaly descends deeply into the mantle transition zone, and the Eastern Alps slab appears detached between 130 and 230 km depth as a result of partial horizontal tearing. The Dinaric slab shows no signs of detachment, but the corresponding high-velocity anomaly

remains relatively narrow, suggesting that the slab may still be intact, hanging on at greater depths.

3.4 Resolution analysis of slab interaction

To assess the model's ability to resolve gaps between slabs, we conducted synthetic tests by introducing two subducting slabs in both the Western and Eastern Alps (Figs. 8 and S15). The slabs were modeled as cylinders: in the W1-W1' cross-section (Fig. 8b) the Western Alps slab dips southeastward at an azimuth of 100°, with a radius of 60 km, while the adjacent Apenninic slab dips northeastward at an azimuth of 40°, with a radius of 50 km. Due to the discretization, the slab model presents jagged boundaries. Similarly, in the E3-E3' cross-section, the Eastern Alps and Dinarides slabs were both modeled with a radius of 50 km, dipping with an azimuth of 10°. High-velocity anomalies of 3% and 5% were assigned to the P-wave and S-wave velocity models, respectively, and a 10% Gaussian white noise was added to the synthetic relative traveltime residuals to simulate high-level noise. Using the same inversion approach, the recovered velocity models were obtained (Fig. 8 and Supplementary Fig. S15). In the recovered models, the amplitude of the velocity anomalies is reduced, and some vertical smearing is present. Nevertheless, the dip directions of the slabs are well-resolved, and the separation between the Western Alps and Apenninic slabs is also clearly discernible by visual inspection.

4. Discussion

4.1. Comparison with previous tomography models and seismic anisotropy data

The analysis of the complex slab structure beneath the greater Alpine region has been the subject of several studies in the past decades, with controversies regarding the site and timing of inferred slab breakoff and/or subduction polarity reversal (e.g., Kissling, 1993; Solarino et al., 1996; Lippitsch et al., 2003; Piromallo and Morelli, 2003; Koulakov et al., 2009; Giacomuzzi et al., 2011; Giacomuzzi et al., 2012; Zhu et al., 2015; Zhao et al., 2016a; Hua et al., 2017; Sun et al., 2019; El- Sharkawy et al., 2020; Kästle et al., 2020; Zhao et al., 2020; Paffrath et al., 2021; Kästle et al., 2022; Rappisi et al., 2022; Kästle et al., 2025). When our results are compared with the recent ray-based P-wave tomography from Paffrath et al. (2021), which utilized data from over 600 seismic stations including the AlpArray Seismic Network (Hetenyi et al., 2018), the main structure of high- and low-velocity anomalies at depths of 150–400 km are largely

consistent (Supplementary Fig. S12). For instance, both Paffrath et al. (2021)'s and our models show a high-velocity anomaly approximately 300 km wide along the A-A' cross-section (Fig. 3a). The main differences between the two models are observed at the uppermost 150 km, likely due to differences in the crustal correction models used, and at depths exceeding 400 km. In fact, Paffrath et al. (2021) utilized earthquakes with epicentral distances of 90–135° that enhance ray coverage at greater depths, whereas our study excluded earthquakes with epicentral distances greater than 90° to minimize arrival-time anomalies caused by potential heterogeneities in the Earth's core. The continuous slab structure documented in our study, from the crust-mantle boundary down to at least 400 km depth, beneath the Alps and the Apennines, is also consistent with the conclusions recently provided for the Alps by Kästle et al. (2025), who utilized a reversible- jump Markov chain Monte Carlo approach to simultaneously constrain the P and S wave velocity structure and their uncertainties in the crust and upper mantle.

However, when compared to previous studies, our tomography models additionally provide evidence of strong interference between the several slabs imaged beneath the greater Alpine region (see the 3D P-wave velocity model in Supplementary file S2). Slab interaction likely conditioned the mantle flow. For example, the upper mantle beneath the Po Plain appears to be trapped between the Alpine, Dinaric and Apenninic slabs, and therefore is not free to move in a toroidal flow, from the rear to the frontal side of the Apennine slab as a response to Apenninic slab retreat, unlike it was proposed by Vignaroli et al. (2008). In that region, our S-wave tomography model shows a prominent low-velocity anomaly between 175 and 300 km depth (Fig. 5a), consistent with previous studies suggesting a region of stationary mantle beneath the Po Plain (Malusà et al., 2018; 2022).

Fundamental information to understand the active mantle flow pattern around the interacting slabs of the greater Alpine region is provided by seismic anisotropy data from low-velocity regions (Barruol et al., 2004; Petrescu et al., 2020; Pondrelli et al., 2024), whereas high-velocity regions could include fossil anisotropic fabrics from within the slabs (Plomerová et al., 2006; Salimbeni et al., 2018; Malusà et al., 2021). Recent studies have revealed variations in the direction and strength of seismic anisotropy at varying depths (Hua et al., 2017; Rappisi et al., 2022; Baccheschi et al., 2024) and have provided evidence for inclined anisotropy (Baccheschi et al., 2024).

Given the potential mutual influences between seismic anisotropy and velocity parameters, we have plotted onto our S-wave velocity model in Fig. 9 the seismic anisotropy from different layers and the dipping anisotropy from splitting intensity (SI) measurements of SKS waves (dt_2 values in Fig. 9a) (Baccheschi et al., 2024). These latter values vary between $dt_2 = 0$, which means horizontal anisotropy, and $dt_2 = 1$, which means inclined anisotropy with dip angle ranging from 30° to 60° (Chevrot, 2000). In the broader region of low-velocity L1 to the west of the Alps, dt_2 values progressively decrease from the west to the east (Fig. 9a). These values suggest a steeply inclined anisotropy in southern France, which becomes progressively less inclined eastward and then horizontal near the Alps-Apennines transition zone. Anisotropy is evidently deflected at 200 km depth around the southern tip of the Western Alps slab (Fig. 9b) and becomes more evidently NW-SE oriented and stronger at 300 km depth (Fig. 9c). Beneath the Po Plain, the anisotropy associated with low-velocity anomaly L2 displays instead NE-SW orientations both in the 200 km and 300 km depth ranges (Fig. 9b,c), and includes a significant vertical component. Strong azimuthal anisotropy with NE-SW direction is found in the 300 km depth range beneath the entire Adriatic microplate, not only in correspondence with anomaly L2, but also in correspondence with anomaly L3. Such NE-SW anisotropy detected all along the Adriatic microplate aligns well with the direction of relative Adria-Europe plate motion inferred from magnetic anomalies since the Late Cretaceous (Dewey et al., 1989; Jolivet and Faccenna, 2000), which suggests that such anisotropic fabric could have formed during post-Jurassic Adria-Europe convergence, and possibly before the onset of Apenninic slab rollback (Salimbeni et al., 2018; Malusà et al., 2021; Baccheschi et al., 2024). However, near the base of the Apenninic slab at 200 km depth, anisotropy directions within the anomaly L3 are oriented N-S and are invariably associated with a vertical component (Fig. 9a). To the west of the Apenninic slab, in correspondence with anomaly L4, seismic anisotropy is slab parallel and horizontal to slightly inclined, which may suggest a toroidal flow in combination with the directions observed within anomaly L3. A horizontal and slab-perpendicular anisotropy direction is instead observed at 100 km depth in the central Apennines (Fig. 9a), which is supportive of the presence of a slab gap right in the place where the P-wave velocity model reveals a reduction in high-velocity anomaly amplitude (Fig. 2a,b), and the S-wave velocity model exhibits a low-velocity anomaly (Fig. 9a).

4.2. Relations between slab interaction and mantle flow

The style of interaction between the Alpine, Apenninic and Dinaric slabs and the surrounding mantle flow based on tomography and seismic anisotropy are summarized in the 3-D interpretive models of Fig. 10. Slab interaction is a direct consequence of the protracted northward motion of the Adriatic microplate relative to Europe since the Late Cretaceous (Dewey et al., 1989; Jolivet and Faccenna, 2000) (Fig. 1a). Previous work suggested that potential interaction between the Alpine and Apenninic slabs could have controlled the position of the northern tip of the fan-shaped Ligurian-Provençal basin (Malusà et al., 2016), and that potential interaction between the Alpine and Dinaric slabs could have determined the tearing of the Alpine slab, thus controlling the composition of Eocene-Oligocene magmatic rocks emplaced near the Giudicare Line (Ji et al., 2019; Mosconi et al., 2024).

In the Alps-Apennines transition zone, slab interaction is now attested by high-resolution tomography data. As shown in Fig. 10a, no gap exists between the two slabs. The asthenospheric mantle L2 beneath the Adriatic plate in the Po Plain has no direct connection with the asthenospheric mantle L1 at the rear of the Alpine slab. In the region of slab interaction, the uppermost part of the SW-dipping Apenninic slab is deformed and becomes NE-dipping (Fig. 10c). It has long been recognized that the Apenninic slab underwent retreat in the Neogene, during its northward motion. Slab retreat should displace, through toroidal flow, part of the underlying mantle from the rear to the front of the retreating slab (Vignaroli et al., 2008; Faccenna and Becker, 2010). However, no toroidal flow can take place in the absence of a suitable slab gap. According to previous studies (Zhao et al., 2016a, Malusà et al., 2021), the absence of a toroidal flow around the northern tip of the retreating Apenninic slab implies that adequate mass compensation is necessarily achieved by the activation of an asthenospheric counterflow to the west of the Alps (red arrow in Fig. 10a). Such counterflow, long recognized based on seismic anisotropy data (e.g., Barruol et al., 2004; Jolivet et al., 2009; Salimbeni et al., 2018), should also include a component of asthenospheric upwelling to compensate the lack of mantle material transferred from the rear to the front of the Apenninic slab (Malusà et al., 2021). The inferred vertical component of the counterflow is confirmed by dt_2 values measured to the west of the Alps (Baccheschi et al., 2024) (Fig. 9a), which suggests a steeply inclined anisotropy in southern France that becomes progressively less inclined eastward and then horizontal in front of the Apenninic slab (Fig. 10a). The mantle upwelling associated with the counterflow is

expected to produce a temperature increase in the upper mantle, which can explain the observed low-velocity anomaly L1 observed both in P- and S-wave tomography models.

Slab interaction is also imaged in the Eastern Alps – Dinarides transition zone (Fig. 10b). Our tomography models reveal that the northward push of the NE-dipping Dinaric slab against the SE-dipping Alpine slab determined a vertical tear in the Alpine slab during the Cenozoic, which became overturned and N-dipping beneath the Eastern Alps. Slab tearing allowed the rise of asthenospheric material, as revealed by a juvenile component in magmatic rocks exposed in the region between the Giudicarie Line and the Veneto Volcanic Province (Ji et al., 2019; Mosconi et al., 2024). However, any potential connection between the asthenospheric mantle located beneath the Po Plain and the asthenospheric mantle located to the north of the Alpine slab remains limited (Fig. 10b). The asthenospheric mantle corresponding to the low-velocity anomaly L2 is sandwiched between the Central Alps slab below and the northern tip of the Adriatic microplate above, and is laterally confined by the Western Alps slab, by the Dinaric slab and by the Apenninic slab (Fig. 10c), with only possible escape towards the SE. In the S-wave tomography model of Fig. 5, the low-velocity anomaly is stronger between 175 and 300 km depth (Fig. 5b) and, according to the higher resolution P-wave tomographic model of Fig. 3b, is strictly associated with the underlying Central Alps slab. These observations support the hypothesis that the low-velocity anomaly L2 is generated by carbon-rich melts in the asthenosphere after the breakdown of slab carbonates and hydrous minerals dragged at depth by the cold Alpine subduction (Malusà et al., 2018, 2022). In fact, carbonates and hydrous minerals can escape breakdown if the geothermal gradient remains lower than 4-5°C/km during subduction, as in the case of the Alps. After subduction, the Alpine slab has been progressively thermally reequilibrated toward ambient mantle conditions and higher temperatures, which promoted dehydration reactions, carbonate breakdown and consequent generation of carbon-rich supercritical fluids at the slab interface. These supercritical fluids triggered melting in the overlying mantle wedge, generating low density and low viscosity carbon-rich melts that rise in the asthenosphere, lowering the observed seismic velocities. The low-velocity anomalies L1 and L2, located on either side of the Alpine slab may thus have different origins, that is asthenospheric upwelling to the west, and fluids released from the Alpine slab to the east beneath the Po Plain (Malusà et al., 2021).Toroidal flow may indeed occur farther south around the

Apenninic slab, in a region where the mantle flow is not controlled by interference between slabs (L3-L4 Fig. 10).

5. Conclusion

The analysis of a high-resolution P-wave velocity model and a new S-wave velocity model reveals the interactions between the several slabs imaged beneath the greater Alpine region and their relationships with prominent low-velocity anomalies in the upper mantle and associated mantle flow. High-velocity anomalies are found beneath the Alps, the Apennines and the northern Dinarides. Prominent low-velocity anomalies are found to the west of the Alps, beneath the Po Plain, and on either side of the central-southern Apennines.

Beneath the Alps-Apennines transition zone, no gap is observed between the interacting Western Alps and Apenninic slabs. The uppermost part of the SW-dipping Apenninic slab is deformed and becomes NE-dipping because of slab interaction. The asthenospheric mantle at the rear of the Alpine slab has no direct connection with the asthenospheric mantle beneath the Po Plain. This precludes any potential toroidal flow around the northern tip of the retreating Apenninic slab. As a result, an asthenospheric counterflow is activated to the west of the Alps to compensate for the lack of mantle material transferred from the rear to the front of the Apenninic slab. Such a counterflow includes a component of asthenospheric upwelling that produces a temperature increase in the upper mantle with consequent decrease in P- and S-wave velocities.

Beneath the Eastern Alps, the NE-dipping Dinaric slab is pushed against the Alpine slab, which is torn and overturned to become N-dipping. Despite slab tearing, no major connection is observed between the asthenospheric mantle located to the north of the Alpine slab and the asthenospheric mantle located beneath the Po Plain, which is bound by slabs and not affected by major flow. The presence of a prominent low-velocity anomaly in that region, strictly associated with the underlying Central Alps slab, supports the hypothesis that the generation of carbon-rich supercritical fluids at the top of the slab triggered melting in the overlying mantle wedge, lowering the observed seismic velocities. Toroidal flow may indeed occur farther south around the Apenninic slab, in a region where the mantle flow is not controlled by interaction between slabs.

We conclude that, because of slab interference, low-velocity anomalies of different origin, either due to asthenospheric upwelling or slab fluids, may coexist in nearby regions of the upper mantle, with major implications for dynamic numerical modeling applied to the analysis of sub-lithospheric mantle convection (e.g., Faccenna and Becker, 2010; Sternai et al., 2019). Our findings may find application to the interpretation of mantle processed in other complex plate-boundary zones, such as Taiwan (Byrne and Liu, 2002) or the Hindu Kush - Pamir - Tianshan tectonic knot in Central Asia (Kufner et al., 2016; Sun et al., 2022), where a complex interplay between opposite-dipping slabs is shown by geophysical and geological data.

Acknowledgments

References

1. Baccheschi, P., Confal, J. M., and Pondrelli, S., 2024, Splitting intensity tomography to image depth-dependent seismic anisotropy patterns beneath the Italian Peninsula and surrounding regions: Earth and Planetary Science Letters, v. 646.
2. Barruol, G., Deschamps, A., & Coutant, O., 2004. Mapping upper mantle anisotropy beneath SE France by SKS splitting indicates Neogene asthenospheric flow induced by Apenninic slab roll-back and deflected by the deep Alpine roots. Tectonophysics, v. 394(1–2), p. 125–138.
3. Byrne, T. B., and Liu, C. S. (Eds.), 2002, Geology and geophysics of an arc-continent collision, Taiwan: Geological Society of America, v. 358.
4. Chevrot, S., 2000. Multichannel analysis of shear wave splitting. J.Geophys. Res. Solid Earth 105, 21579–21590. https://doi.org/10.1029/2000JB900199. B9.
5. Closs, H., and Y. Labrouste (Eds.), 1963, Rechèrches Séismologiques Dans les Alpes Occidentales au Moyen de Grandes Explosions en 1956, 1958 et 1960: Mem. Coll. Année Geophys. Int. Ser., vol. 12-2, 241 p., Cent. for Natl. Res. Sci., Paris.
6. Dahlen, F. A., Hung, S. H., and Nolet, G., 2000, Fréchet kernels for finite-frequency traveltimes-I. Theory: Geophysical Journal International, v. 141, no. 1, p. 157-174.
7. Dewey, J. F., Helman, M. L., Knott, S. D., Turco, E., and Hutton, D. H. W., 1989, Kinematics of the western Mediterranean: Geological Society, London, Special Publications, v. 45, no. 1, p. 265-283.
8. El- Sharkawy, A., Meier, T., Lebedev, S., Behrmann, J. H., Hamada, M., Cristiano, L., Weidle, C., and Köhn, D., 2020, The Slab Puzzle of the Alpine- Mediterranean Region: Insights From a New, High- Resolution, Shear Wave Velocity Model of the Upper Mantle: Geochemistry, Geophysics, Geosystems, v. 21, no. 8.
9. Eva, E., Malusà, M. G., and Solarino, S., 2020, Seismotectonics at the transition between opposite- dipping slabs (western Alpine region). Tectonics, v. 39(9), e2020TC006086.
10. Faccenna, C., and Becker, T. W., 2010, Shaping mobile belts by small-scale convection: Nature, v. 465(7298), p. 602-605.

11. Gattacceca, J., A. Deino, R. Rizzo, D.S. Jones, B. Henry, B. Beaudoin, and F. Vadeboin, 2007, Miocene rotation of Sardinia: New paleomagnetic and geochronological constraints and geodynamic implications: Earth and Planetary Science Letters, v. 258, p. 359-377.

12. Giacomuzzi, G., Chiarabba, C., and De Gori, P., 2011, Linking the Alps and Apennines subduction systems: New constraints revealed by high-resolution teleseismic tomography: Earth and Planetary Science Letters, v. 301, no. 3-4, p. 531-543.

13. Giacomuzzi, G., Civalleri, M., De Gori, P., and Chiarabba, C., 2012, A 3D Vs model of the upper mantle beneath Italy: Insight on the geodynamics of central Mediterranean: Earth and Planetary Science Letters, v. 335-336, p. 105-120.

14. Handy, M. R., M. Schmid, S., Bousquet, R., Kissling, E., and Bernoulli, D., 2010, Reconciling plate-tectonic reconstructions of Alpine Tethys with the geological–geophysical record of spreading and subduction in the Alps: Earth-Science Reviews, v. 102, no. 3–4, p. 121–158.

15. Handy, M. R., Schmid, S. M., Paffrath, M., and Friederich, W., 2021, Orogenic lithosphere and slabs in the greater Alpine area – interpretations based on teleseismic P-wave tomography: Solid Earth, v. 12, no. 11, p. 2633-2669.

16. Hetenyi, G., Molinari, I., Clinton, J., Bokelmann, G., Bondar, I., Crawford, W. C., Dessa, J. X., Doubre, C., Friederich, W., Fuchs, F., Giardini, D., Graczer, Z., Handy, M. R., Herak, M., Jia, Y., Kissling, E., Kopp, H., Korn, M., Margheriti, L., Meier, T., Mucciarelli, M., Paul, A., Pesaresi, D., Piromallo, C., Plenefisch, T., Plomerova, J., Ritter, J., Rumpker, G., Sipka, V., Spallarossa, D., Thomas, C., Tilmann, F., Wassermann, J., Weber, M., Weber, Z., Wesztergom, V., Zivcic, M., AlpArray Seismic Network, T., AlpArray, O. B. S. C. C., and AlpArray Working, G., 2018, The AlpArray Seismic Network: A Large-Scale European Experiment to Image the Alpine Orogen: Surv Geophys, v. 39, no. 5, p. 1009-1033.

17. Hua, Y., Zhao, D., and Xu, Y., 2017, P wave anisotropic tomography of the Alps: Journal of Geophysical Research: Solid Earth, v. 122, no. 6, p. 4509-4528.

18. Hung, S. H., Dahlen, F. A., and Nolet, G., 2000, Fréchet kernels for finite-frequency traveltimes-II. Examples: Geophysical Journal International, v. 141, no. 1, p. 175-203.

19. Ji, W. Q., Malusà, M. G., Tiepolo, M., Langone, A., Zhao, L., and Wu, F. Y., 2019, Synchronous Periadriatic magmatism in the Western and Central Alps in the absence of slab breakoff: Terra Nova, v. 31, no. 2, p. 120–128.

20. Jolivet, L., and Faccenna, C., 2000, Mediterranean extension and the Africa-Eurasia collision: Tectonics, v. 19, no. 6, p. 1095-1106.

21. Jolivet, L., Faccenna, C., and Piromallo, C., 2009: From mantle to crust: Stretching the Mediterranean: Earth and Planetary Science Letters, v. 285(1-2), p. 198-209.

22. Jozi Najafabadi, A., Haberland, C., Le Breton, E., Handy, M. R., Verwater, V. F., Heit, B., and Weber, M., 2022, Constraints on Crustal Structure in the Vicinity of the Adriatic Indenter (European Alps) From Vp and Vp/Vs Local Earthquake Tomography: Journal of Geophysical Research: Solid Earth, v. 127, no. 2.

23. Kästle, E. D., El-Sharkawy, A., Boschi, L., Cristiano, L., and Weidle, C., 2018, SurfaceWave Tomography of the Alps Using Ambient-Noise and Earthquake Phase Velocity Measurements: Journal of Geophysical Research: Solid Earth, v. 123, p. 1770–1792.

24. Kästle, E. D., Rosenberg, C., Boschi, L., Bellahsen, N., Meier, T., and El-Sharkawy, A., 2020, Slab breakoffs in the Alpine subduction zone: International Journal of Earth Sciences, v. 109, no. 2, p. 587–603.

25. Kästle, E. D., Molinari, I., Boschi, L., and Kissling, E., 2022, Azimuthal anisotropy from eikonal tomography: example from ambient-noise measurements in the AlpArray network: Geophysical Journal International, v. 229, no. 1, p. 151-170.

26. Kästle, E. D., Paffrath, M., El- Sharkawy, A., & AlpArray and Swath- D working groups, 2025. Alpine Crust and Mantle Structure From 3D Monte Carlo Surface- and Body- Wave Tomography. Journal of Geophysical Research: Solid Earth, v. 130(2), e2024JB030101.

27. Kennett, B. L. N., and Engdahl, E. R., 1991, Traveltimes for global earthquake location and phase identification: Geophysical Journal International, v. 105, p. 429-465.

28. Kind, R., Schmid, S. M., Schneider, F., Meier, T., Yuan, X., Heit, B., and Schiffer, C., 2023, Sp converted waves reveal the structure of the lithosphere below the Alps and their northern foreland: Geophysical Journal International, v. 235, no. 2, p. 1832-1848.

29. Kissling, E., 1993, Deep structure of the Alps—what do we really know?: Physics of the Earth and Planetary Interiors, v. 79, no. 1-2, p. 87-112.

30. Koulakov, I., Kaban, M. K., Tesauro, M., and Cloetingh, S., 2009, P- and S-velocity anomalies in the upper mantle beneath Europe from tomographic inversion of ISC data: Geophysical Journal International, v. 179, no. 1, p. 345-366.

31. Kufner, S. K., Schurr, B., Sippl, C., Yuan, X., Ratschbacher, L., Ischuk, A., Murodkulov, S., Schneider, F., Mechie, J., and Tilmann, F., 2016, Deep India meets deep Asia: Lithospheric indentation, delamination and break-off under Pamir and Hindu Kush (Central Asia): Earth and Planetary Science Letters, v. 435, p. 171-184.

32. Lévěque, J.-J., Rivera, L., and Wittlinger, G., 1993, On the use of the checker-board test to assess the resolution of tomographic inversions: Geophysical Journal International, v. 115, no. 1, p. 313-318.

33. Lippitsch, R., Kissling, E., and Ansorge, J., 2003, Upper mantle structure beneath the Alpine orogen from high- resolution teleseismic tomography: Journal of Geophysical Research: Solid Earth, v. 108, no. B8.

34. Lu, Y., Stehly, L., Brossier, R., Paul, A., and Group, A. W., 2020, Imaging Alpine crust using ambient noise wave-equation tomography: Geophysical Journal International, v. 222, no. 1, p. 69-85.

35. Malusà, M. G., Faccenna, C., Baldwin, S. L., Fitzgerald, P. G., Rossetti, F., Balestrieri, M. L., Ellero, A., Ottria, G., and Piromallo, C., 2015, Contrasting styles of (U) HP rock exhumation along the Cenozoic Adria- Europe plate boundary (Western Alps, Calabria, Corsica): Geochemistry, Geophysics, Geosystems, v. 16(6), p. 1786-1824.

36. Malusà, M. G., Anfinson, O. A., Dafov, L. N., and Stockli, D. F., 2016, Tracking Adria indentation beneath the Alps by detrital zircon U-Pb geochronology: Implications for the Oligocene–Miocene dynamics of the Adriatic microplate: Geology, v. 44(2), p. 155-158.

37. Malusà, M. G., Frezzotti, M. L., Ferrando, S., Brandmayr, E., Romanelli, F., and Panza, G. F., 2018, Active carbon sequestration in the Alpine mantle wedge and implications for long-term climate trends. Scientific reports, v. 8(1), 4740.

38. Malusà, M. G., Brandmayr, E., Panza, G. F., Romanelli, F., Ferrando, S., and Frezzotti, M. L., 2022, An explosive component in a December 2020 Milan earthquake suggests outgassing of deeply recycled carbon: Communications Earth & Environment, v. 3, no. 1.

39. Malusà, M. G., Guillot, S., Zhao, L., Paul, A., Solarino, S., Dumont, T., Schwartz, S., Aubert, C., Baccheschi, P., Eva, E., Lu, Y., Lyu, C., Agostinetti, N. P., Pondrelli, S., Salimbeni, S., Sun, W.,

and Yuan, H., 2021, The deep structure of the Alps based on the CIFALPS seismic experiment: A synthesis: Geochemistry, Geophysics, Geosystems, v. 22, p. e2020GC009466.

40. Monna, S., Montuori, C., Frugoni, F., Piromallo, C., and Vinnik, L., 2022, Moho and LAB Across the Western Alps (Europe) From P and S Receiver Function Analysis: Journal of Geophysical Research: Solid Earth, v. 127, no. 10.

41. Mosconi, A., Cannaò, E., Farina, F., Malusà, M. G., Zanchetta, S., and Tiepolo, M., 2024, The Corno Alto complex (Adamello batholith): A modern analogue of the high Ba/K sanukitoids: Lithos, v. 470, 107522.

42. Nouibat, A., Stehly, L., Paul, A., Schwartz, S., Bodin, T., Dumont, T., Rolland, Y., and Brossier, R., 2022, Lithospheric transdimensional ambient-noise tomography of W-Europe: implications for crustal-scale geometry of the W-Alps: Geophysical Journal International, v. 229, no. 2, p. 862–879.

43. Nouibat, A., Brossier, R., Stehly, L., Cao, J., and Paul, A., 2023, Ambient- Noise Wave- Equation Tomography of the Alps and Ligurian- Provence Basin: Journal of Geophysical Research: Solid Earth, v. 128, no. 10.

44. Paffrath, M., Friederich, W., Schmid, S. M., and Handy, M. R., 2021, Imaging structure and geometry of slabs in the greater Alpine area – a P-wave travel-time tomography using AlpArray Seismic Network data: Solid Earth, v. 12, no. 11, p. 2671–2702.

45. Paige, C. C., and Saunders, M. A., 1982, LSQR: An Algorithm for Sparse Linear Equations and Sparse Least Squares: Association for Computing Machinery, v. 8.

46. Paul, A., Malusà, M. G., Solarino, S., Salimbeni, S., Eva, E., Nouibat, A., Pondrelli, S., Aubert, C., Dumont, T., Guillot, S., Schwartz, S., and Zhao, L., 2022, Along-strike variations in the fossil subduction zone of the Western Alps revealed by the CIFALPS seismic experiments and their implications for exhumation of (ultra-) high-pressure rocks: Earth and Planetary Science Letters, v. 598, p. 117843.

47. Petrescu, L., Pondrelli, S., Salimbeni, S., and Faccenda, M., 2020, Mantle flow below the central and greater Alpine region: insights from SKS anisotropy analysis at AlpArray and permanent stations: Solid Earth, v. 11, no. 4, p. 1275-1290.

48. Piromallo, C., and Morelli, A., 2003, P wave tomography of the mantle under the Alpine- Mediterranean area: Journal of Geophysical Research: Solid Earth, v. 108, no. B2.

49. Plomerová, J., Margheriti, L., Park, J., Babuška, V., Pondrelli, S., Vecsey, L., Piccinini, D., Levin, V., Baccheschi, P., and Salimbeni, S., 2006. Seismic anisotropy beneath the Northern Apennines (Italy): Mantle flow or lithosphere fabric? Earth and Planetary Science Letters, v. 247(1-2), p. 157-170.

50. Pondrelli, S., Salimbeni, S., Confal, J. M., Malusà, M., Paul, A., Guillot, S., Solarino, S., Eva, E., Aubert, C., and Zhao, L., 2024, Highlights on mantle deformation beneath the Western Alps with seismic anisotropy using CIFALPS2 data.

51. Rappisi, F., VanderBeek, B. P., Faccenda, M., Morelli, A., and Molinari, I., 2022, Slab Geometry and Upper Mantle Flow Patterns in the Central Mediterranean From 3D Anisotropic P- Wave Tomography: Journal of Geophysical Research: Solid Earth, v. 127, no. 5.

52. Rawlinson, N., and Sambridge, M., 2003, Seismic Traveltime Tomography of the Crust and Lithosphere: Advances in Geophysics, v. 46, p. 81-197.

53. Salimbeni, S., Malusà, M. G., Zhao, L., Guillot, S., Pondrelli, S., Margheriti, L., Paul, A., Solarino, S., Aubert, C., Dumont, T., Schwartz, S., Wang, Q., Xu, X., Zheng, T., and Zhu, R., 2018, Active

and fossil mantle flows in the western Alpine region unravelled by seismic anisotropy analysis and high-resolution P wave tomography: Tectonophysics, v. 731–732, p. 35–47.

54. Solarino, S., Malusà, M. G., Eva, E., Guillot, S., Paul, A., Schwartz, S., Zhao, L., Aubert, C., Dumont, T., Pondrelli, S., Salimbeni, S., Wang, Q., Xu, X., Zheng, T., and Zhu, R., 2018, Mantle wedge exhumation beneath the Dora-Maira (U)HP dome unravelled by local earthquake tomography (Western Alps): Lithos, v. 296–299, p. 623–636.

55. Solarino, S., Malusà, M. G., Eva, E., Paul, A., Guillot, S., Pondrelli, S., Salimbeni, S., and Zhao, L., 2024. Seismic tomography reveals contrasting styles of subduction-channel and mantle-wedge exhumation controlled by upper plate divergent motion. Gondwana Research, v. 136, p. 169-182.

56. Solarino, S., Spallarossa, D., Parolai, S., Cattaneo, M., and Eva, C., 1996, Litho—asthenospheric structures of northern Italy as inferred from teleseismic P-wave tomography: Tectonophysics, v. 260, no. 4, p. 271-289.

57. Sternai, P., Sue, C., Husson, L., Serpelloni, E., Becker, T. W., Willett, S. D., Faccenna, C., Di Giulio, A., Spada, G., Jolivet, L., Valla, P., Petit, C., Nocquet, J.-M., Walpersdorf, A., and Castelltort, S., 2019, Present-day uplift of the European Alps: Evaluating mechanisms and models of their relative contributions: Earth-Science Reviews, v. 190, p. 589-604.

58. Sun, W., Zhao, L., Malusà, M. G., Guillot, S., and Fu, L., 2019, 3-D Pn tomography reveals continental subduction at the boundaries of the Adriatic microplate in the absence of a precursor oceanic slab: Earth and Planetary Science Letters, v. 510, p. 131–141.

59. Sun, W., Ao, S., Tang, Q., Malusà, M. G., Zhao, L., and Xiao, W., 2022, Forced Cenozoic continental subduction of Tarim craton-like lithosphere below the Tianshan revealed by ambient noise tomography: Geology, v. 50(12), p. 1393-1397.

60. VanDecar, J. C., and Crosson, R. S., 1990, Determination of teleseismic relative phase arrival times using multi-channel cross-correlation and least squares: Bulletin of the Seismological Society of America, v. 80, no. 1, p. 150-169.

61. Vignaroli, G., Faccenna, C., Jolivet, L., Piromallo, C., and Rossetti, F., 2008. Subduction polarity reversal at the junction between the Western Alps and the Northern Apennines, Italy. Tectonophysics, v. 450(1-4), p. 34-50.

62. Yu, C., Zheng, Y., and Shang, X., 2017, Crazyseismic: A MATLAB GUI- Based Software Package for Passive Seismic Data Preprocessing: Seismological Research Letters, v. 88, no. 2A, p. 410-415.

63. Zhao, L., Paul, A., Malusà, M. G., Xu, X., Zheng, T., Solarino, S., Guillot, S., Schwartz, S., Dumont, T., Salimbeni, S., Aubert, C., Pondrelli, S., Wang, Q., and Zhu, R., 2016a, Continuity of the Alpine slab unraveled by high-resolution P wave tomography: Journal of Geophysical Research: Solid Earth, v. 121, no. 12, p. 8720–8737.

64. Zhao, L., Paul, A., and Solarino, S., 2016b, Seismic network YP: CIFALPS temporary experiment (China-Italy-France Alps seismic transect): RESIF - Réseau Sismologique et géodésique Français.

65. Zhao, L., Paul, A., Solarino, S., and RESIF, 2018, Seismic network XT: CIFALPS-2 temporary experiment (China-Italy-France Alps seismic transect #2: RESIF - Réseau Sismologique et géodésique Français.

66. Zhao, L., Malusà, M. G., Yuan, H., Paul, A., Guillot, S., Lu, Y., Stehly, L., Solarino, S., Eva, E., Lu, G., and Bodin, T., 2020, Evidence for a serpentinized plate interface favouring continental subduction: Nature Communications, v. 11, no. 1, p. 2171.

67. Zhu, H., Bozdağ, E., and Tromp, J., 2015, Seismic structure of the European upper mantle based on adjoint tomography: Geophysical Journal International, v. 201, no. 1, p. 18–52.

Supplementary Table S1 The number of events and traveltime residuals of P and S waves in different frequency band

	P (0.1-0.5 Hz)	P (0.5-2 Hz)	S (0.05-0.1 Hz)	S (0.1-0.5 Hz)
Number of Events	454	405	303	153
Number of Residuals	114173	103636	79181	25636

I would put this table in the supplementary material so as not to exceed the maximum number of figures+tables allowed by EPSL

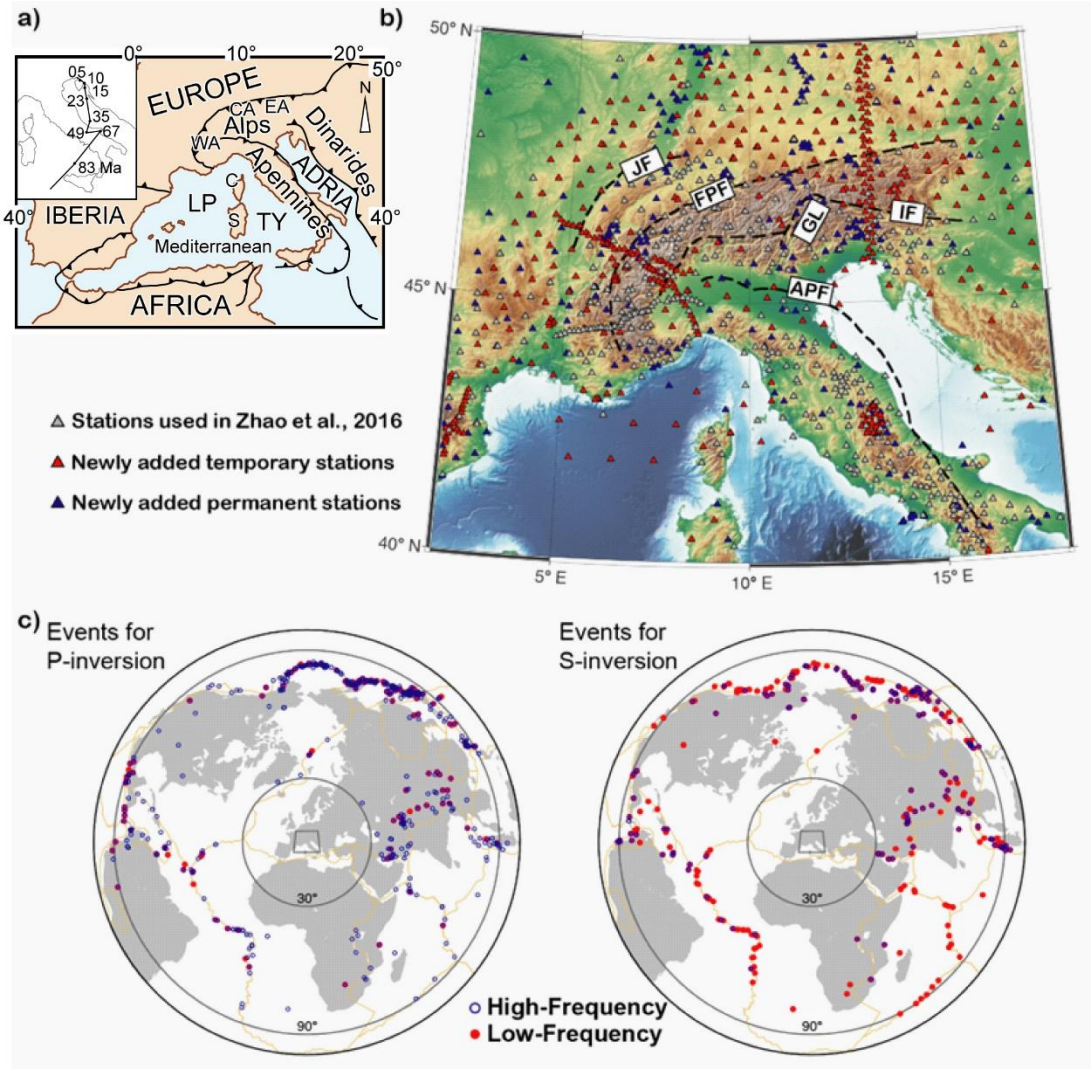

Figure 1. Tectonic setting, seismic stations and event distribution for P and S wave finite-frequency tomography. **(a)** Tectonic sketch map of the study area and relative motion of the Adriatic microplate relative to Europe since the Late Cretaceous (after Dewey et al., 1989; Jolivet and Faccenna, 2000). Acronyms: WA, Western Alps; CA, Central Alps; EA, Eastern Alps; C, Corsica; S, Sardinia; LP, Ligurian-Provençal Basin; TY, Tyrrhenian Basin. **(b)** Seismic station distribution on topography map. The gray triangles indicate stations from previous studies (Zhao et al., 2016a), the red and blue triangles indicate the newly added temporary and permanent stations of this study. Main tectonic boundaries (black dashed lines): FPF, Frontal Pennine Fault; APF, Apennines Front; IF, Insubric Fault; GL, Giudicarie Line; JF, Jura Front. **(c)** Events distribution for P- and S-wave inversion used in this study. The blue circles denote the selected events of high frequency (P: 0.5~2 Hz, S: 0.1~0.5 Hz), the red dots denote selected events of low

frequency (P: 0.1~0.5 Hz, S: 0.05~0.1 Hz). The brown lines indicate major plate boundaries. The gray rectangle marks the study area.

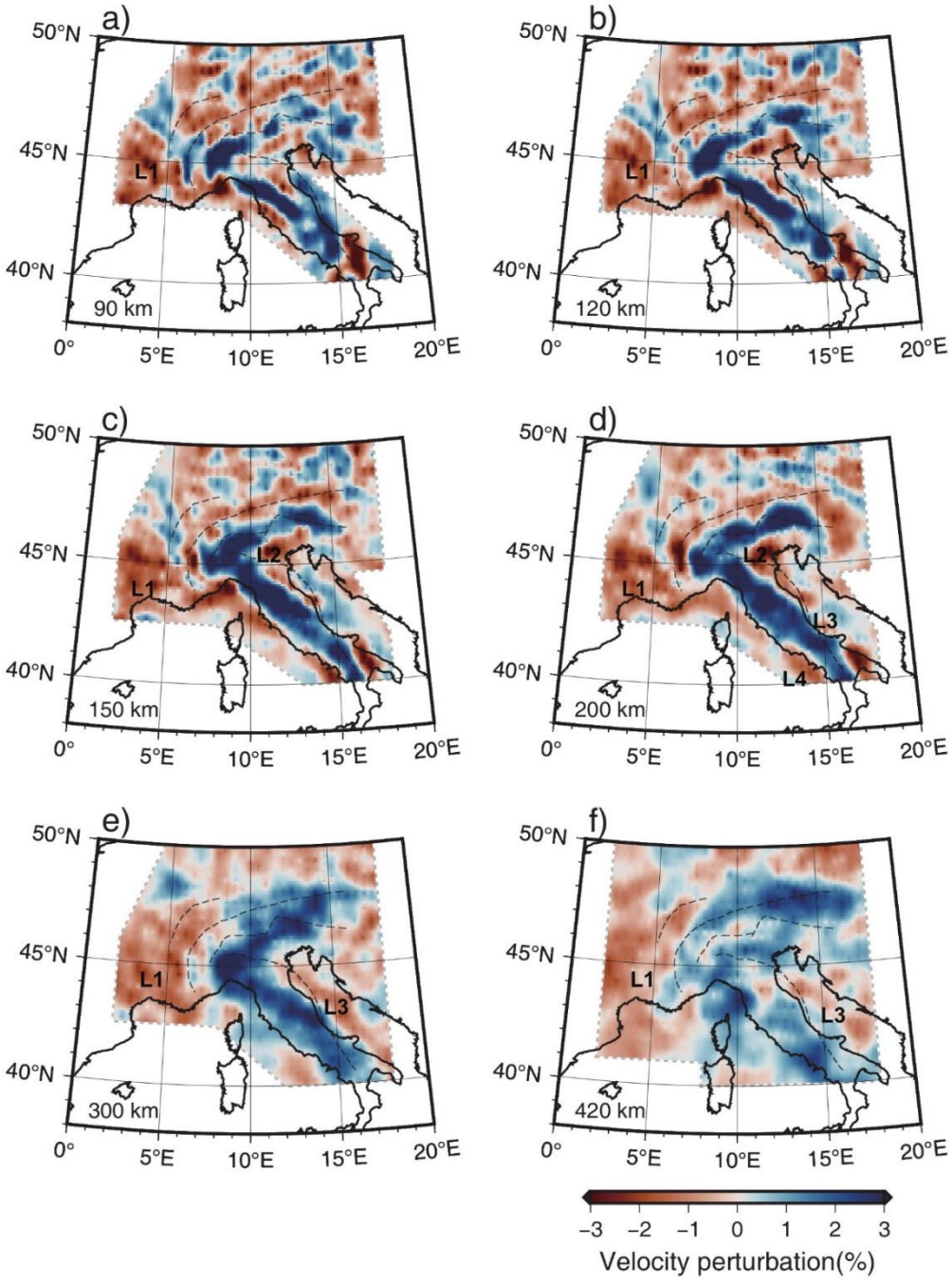

Figure 2. Depth slices of the P-wave velocity perturbation model at different depths. The gray dashed lines mark the outlines of the well-resolved areas estimated from resolution tests (Figure S9). Main tectonic boundaries (grey dashed lines) as in Figure 1b. L1 to L4 indicate the main low-velocity anomalies discussed in the text.

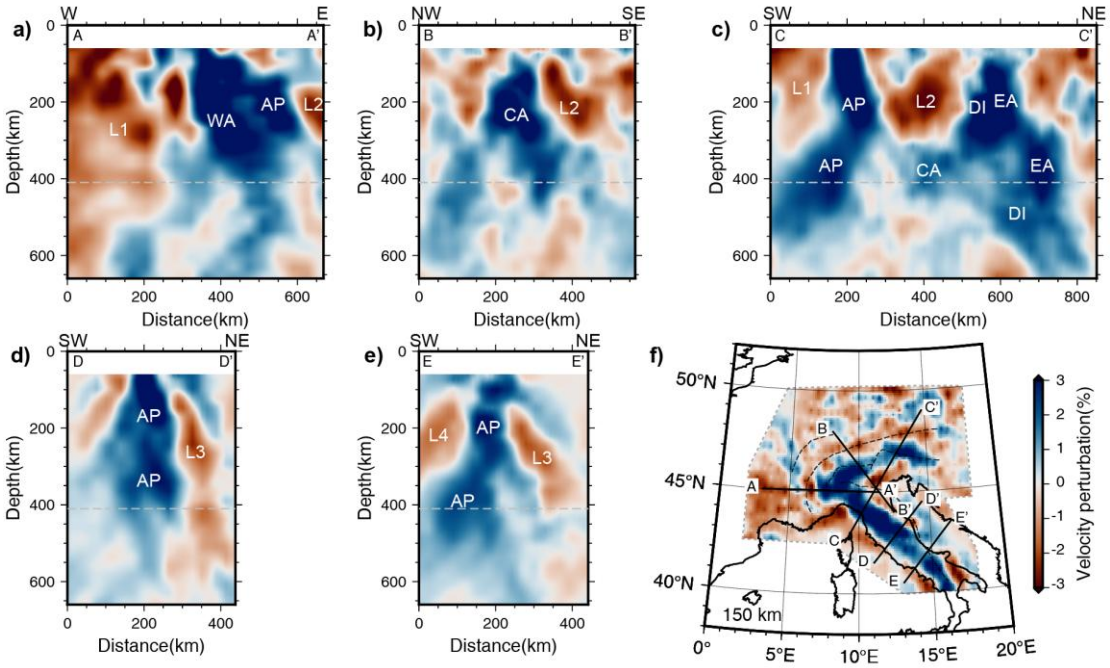

Figure 3. Cross sections of the P-wave velocity perturbation model (a-e). Cross-section locations are indicated on the 150 km depth slice of the P-wave velocity model **(f)**. High-velocity anomalies are labeled as follows: WA (Western Alps), CA (Central Alps), EA (Eastern Alps), DI (Dinarides), AP (Apennines). L1 to L4 mark the main low-velocity anomalies discussed in the text.

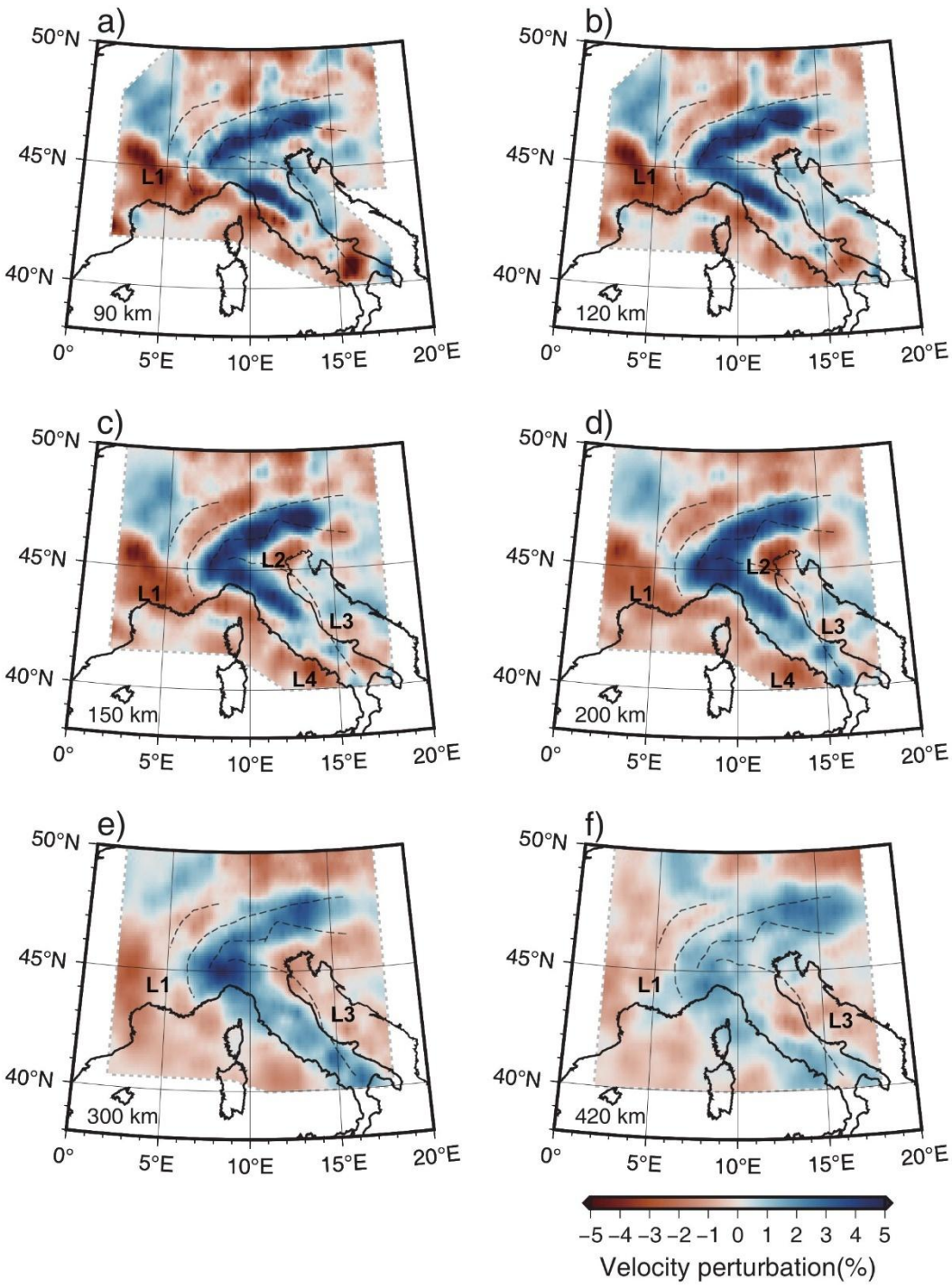

Figure 4. Depth slices of the S-wave velocity perturbation model at different depths. The gray dashed lines mark the outlines of the well-resolved areas estimated from resolution tests (Figure S11). Main tectonic boundaries (grey dashed lines) as in Figure 1b. L1 to L4 indicate the main low-velocity anomalies discussed in the text.

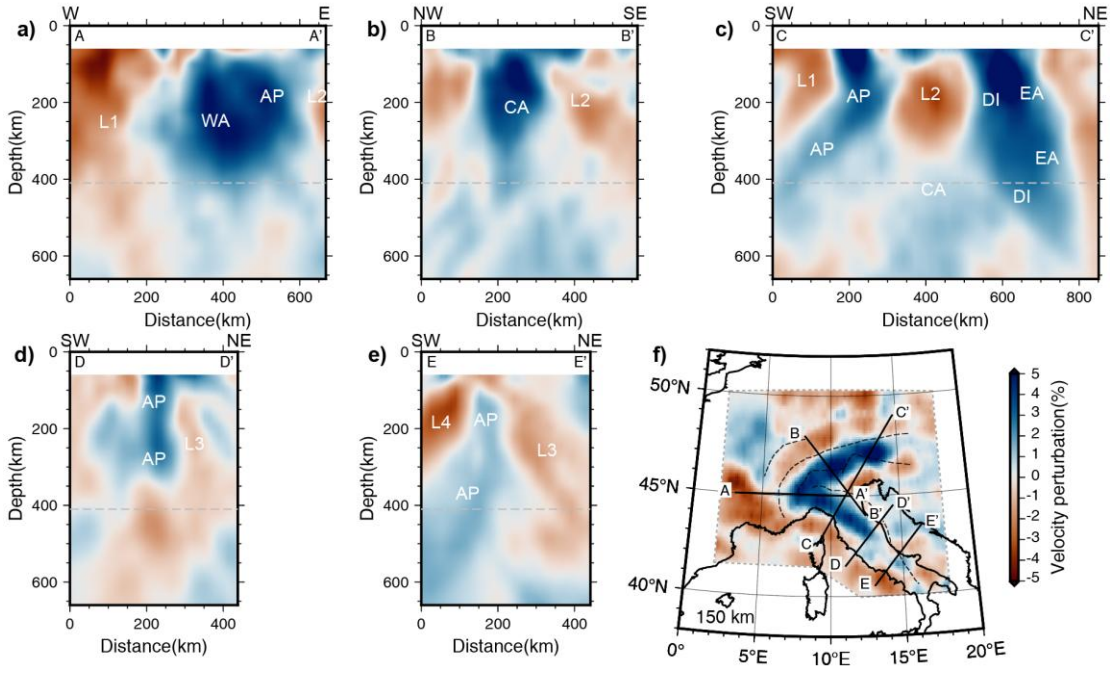

Figure 5. Cross sections of the S-wave velocity perturbation model (a-e). Cross-section locations are indicated on the 150 km depth slice of the S-wave velocity model **(f)**. High-velocity anomalies are labeled as follows: WA (Western Alps), CA (Central Alps), EA (Eastern Alps), DI (Dinarides), AP (Apennines). L1 to L4 mark the main low-velocity anomalies discussed in the text.

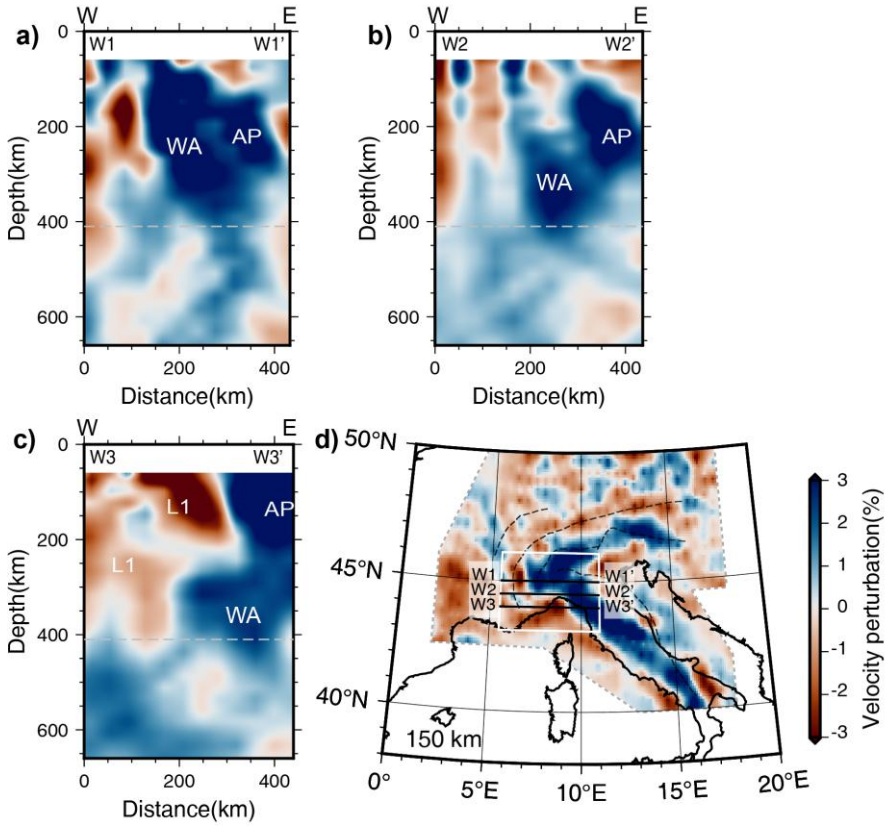

Figure 6. Cross-sections of the Western Alps - Apennines transition zone. **(a-c)** P-wave velocity cross sections. **(d)** Cross-section locations on the 150 km depth slice of the P-wave velocity perturbation model. AP: Apennines, WA: Western Alps.

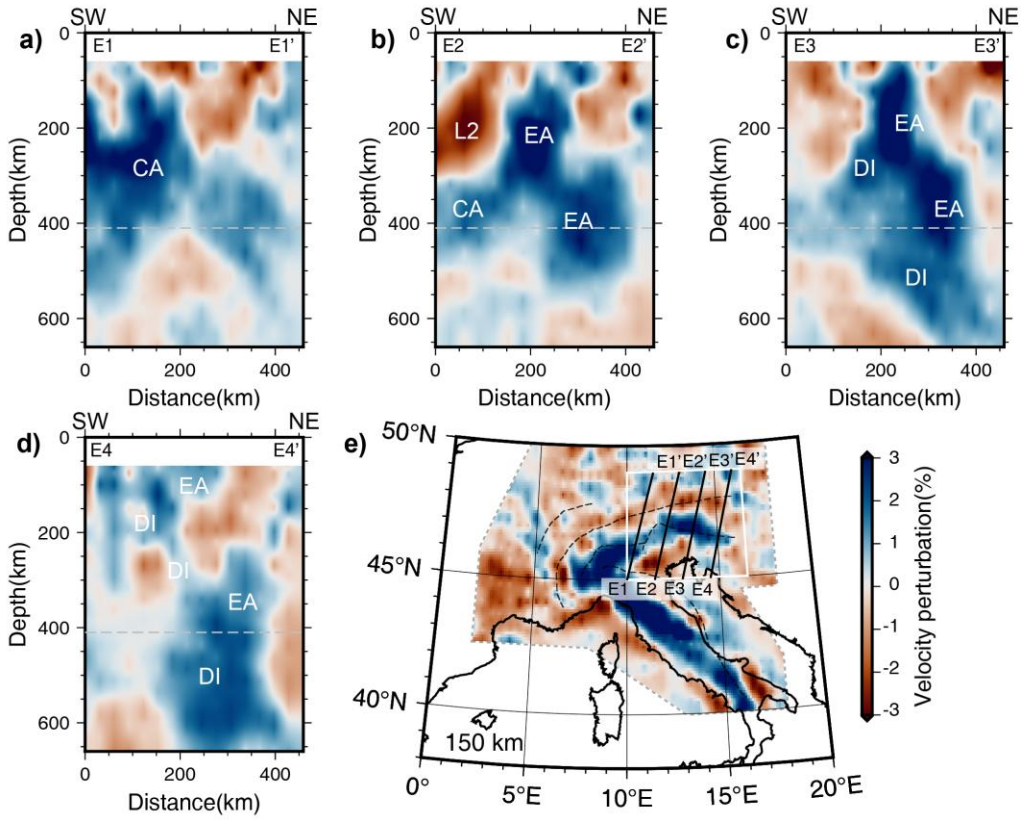

Figure 7. Cross-sections of the Eastern Alps – Dinarides transition zone. **(a-d)** P-wave velocity cross sections. **(e)** Cross-section locations on the 150 km depth slice of the P-wave velocity perturbation model. CA: Central Alps, EA: Eastern Alps, DI: Dinarides.

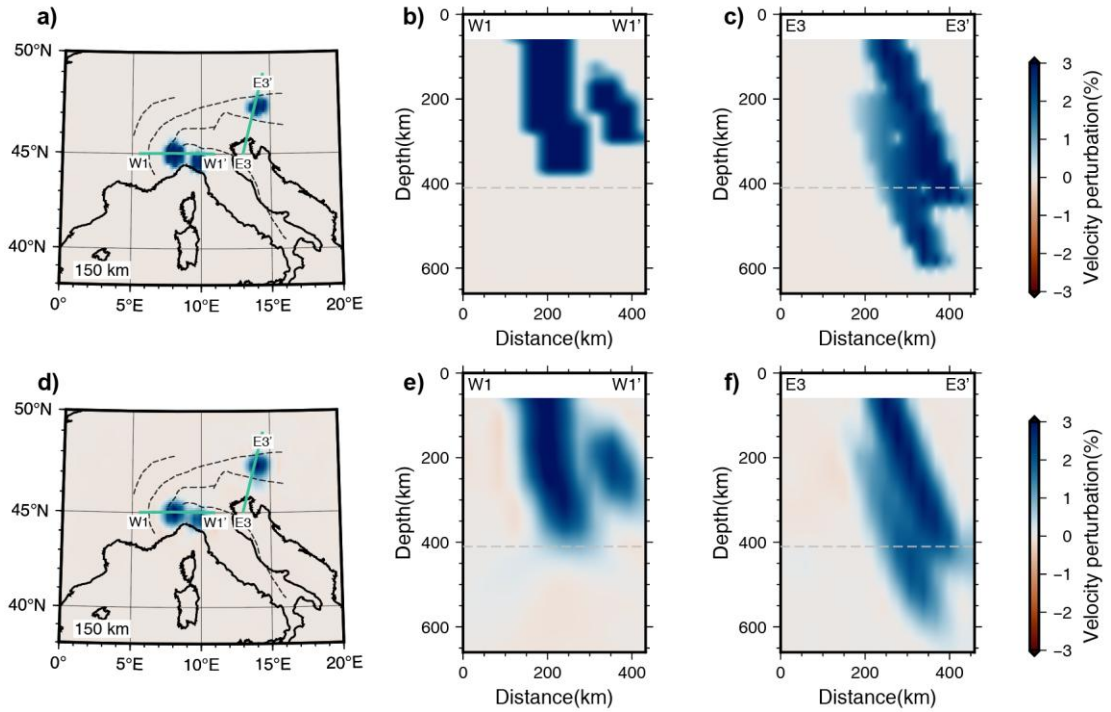

Figure 8. Resolution analysis of slab interaction. (a-c) The input model includes four high-velocity anomalies with a 3% increase in P-wave velocity in the upper mantle, designed to represent the slabs of the Western Alps, the Eastern Alps, the Apennines, and the Dinarides. The cross-sections in (b) and (c) correspond to and are labelled as those shown in Figures 6 and 7. **(d-f)** Recovered velocity models.

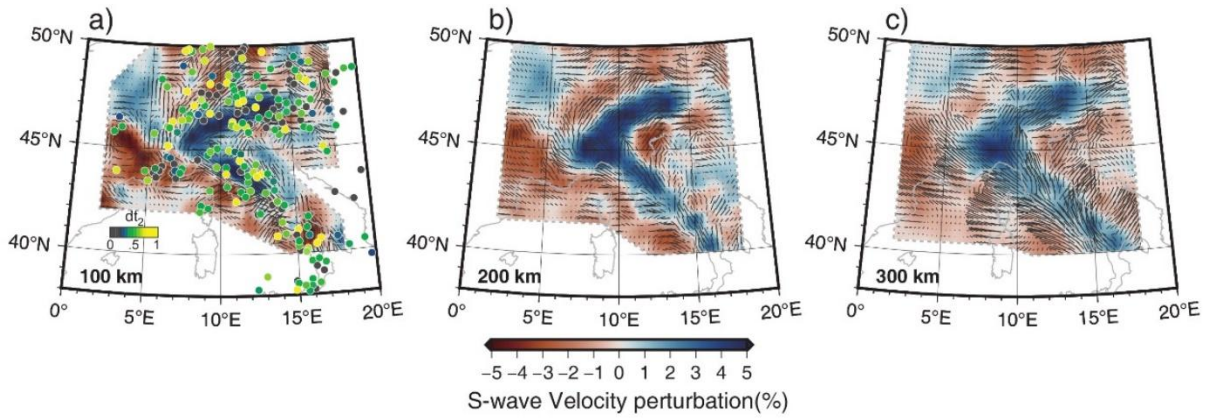

Figure 9. Relationships between S-wave velocity anomalies and seismic anisotropy. (a) S-wave velocity perturbation at 100 km depth (this work) and dt_2 values (color-coded circles, from Baccheschi et al., 2024) which is a theoretical indicator for inclined anisotropy (gray = horizontal; yellow = 60° dip). **(b-c)** S-wave velocity anomalies (this work) and shear wave anisotropy at 200 and 300 km depth (black bars, their length is proportional to the modulus of shear wave anisotropy, from Baccheschi et al., 2024).

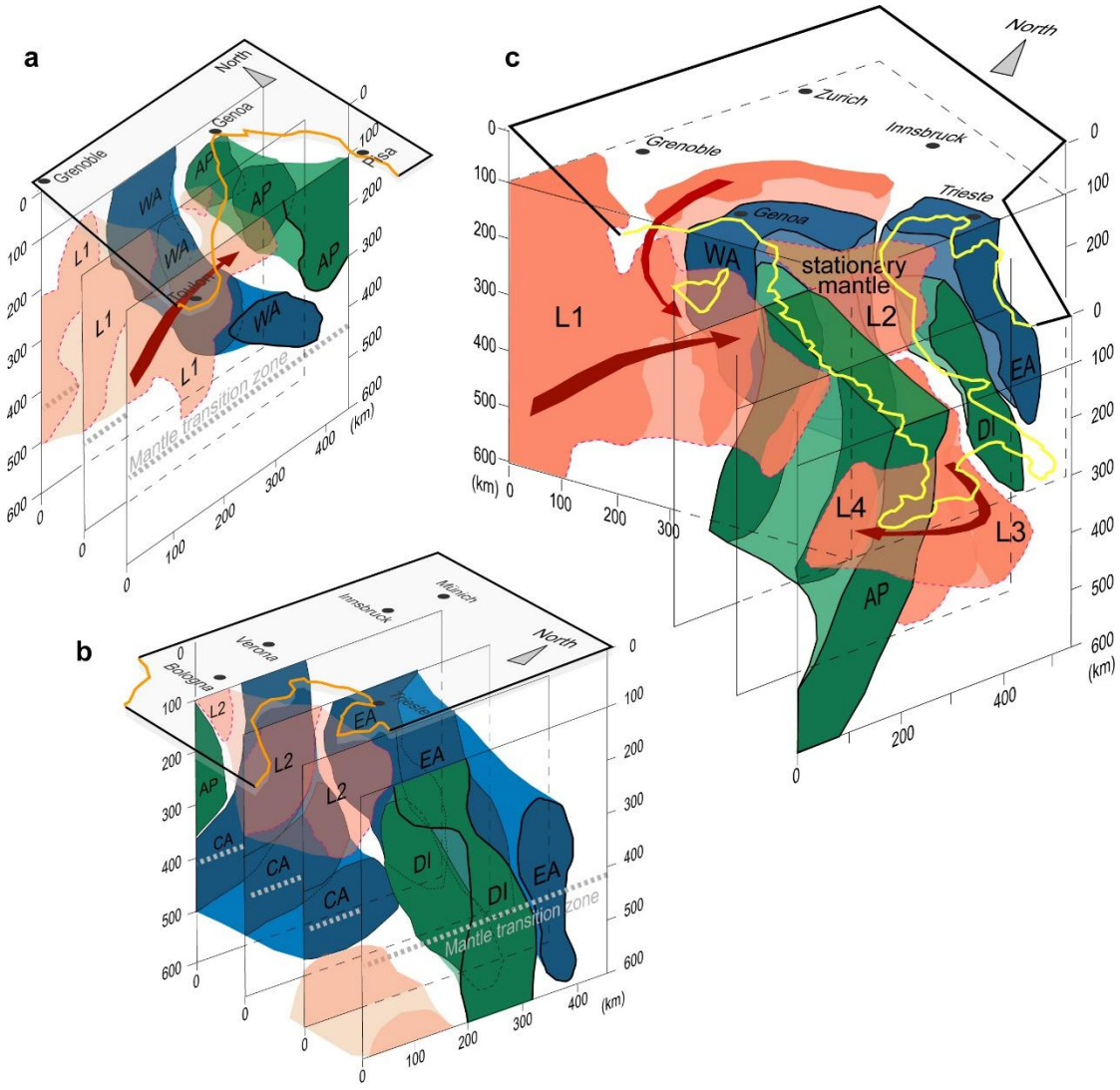

Figure 10. 3-D interpretive models of slab interference and mantle flow beneath the great Alpine region. (a) Interference between the Apenninic slab and the Western Alps slab based on the cross-sections in Figure 6. **(b)** Interference between the Dinaric slab and the Central and Eastern Alps slabs based on the cross-sections in Figure 7. **(c)** Mantle flows (red arrows) around the slabs beneath the greater Alpine region based on cross-sections in Figs. 3 and 5. L1-L4 indicate the main low-velocity anomalies in the mantle. Slabs: AP = Apennines; CA = Central Alps; DI = Dinarides; EA = Eastern Alps; WA = Western Alps.